Adsorption of Flavonoids in a Transcriptional Regulator TtgR: Relative Binding Free Energies and Intermolecular Interactions

Yuxuan Wu, Shi Zhang, Darrin M. York, and Lu Wang*

ACCESS | Metrics & More | Article Recommendations | Supporting Information

ABSTRACT: Antimicrobial resistance in bacteria often arises from their ability to actively identify and expel toxic compounds. The bacterium strain *Pseudomonas putida* DOT-T1E utilizes its TtgABC efflux pump to confer robust resistance against antibiotics, flavonoids, and organic solvents. This resistance mechanism is intricately regulated at the transcriptional level by the TtgR protein. Through molecular dynamics and alchemical free energy simulations, we systematically examine the binding of seven flavonoids and their derivatives with the TtgR transcriptional regulator. Our simulations reveal distinct binding geometries and free energies for the flavonoids in the active site of the protein, which are driven by a range of noncovalent forces encompassing van der Waals, electrostatic, and hydrogen bonding interactions. The interplay of molecular structures, substituent patterns, and intermolecular interactions effectively stabilizes the bound flavonoids, confining their movements within the TtgR binding pocket. These findings yield valuable insights into the molecular determinants that govern ligand recognition in TtgR and shed light on the mechanism of antimicrobial resistance in *P. putida* DOT-T1E.
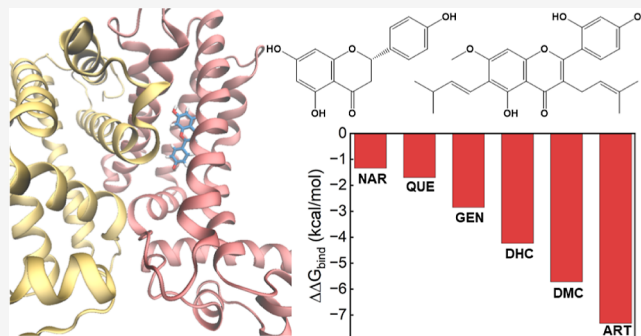
INTRODUCTION

Antimicrobial resistance presents a significant global health challenge as bacteria utilize diverse mechanisms to counteract the effects of antimicrobial agents. Among these strategies, efflux pumps, a class of transmembrane transporter proteins, play a crucial role. Efflux pumps actively recognize and expel antimicrobial agents from bacterial cells, thereby facilitating their adaptive survival mechanisms.[1−4] For example, the Gram-negative bacterium *Pseudomonas putida* strain DOT-T1E utilizes three homologous efflux pumps—TtgABC, TtgDEF, and TtgGHI—to grow in the presence of antibiotics, flavonoids, and toxic organic solvents.[5−9] Notably, TtgABC acts as a major contributor to multidrug resistance and its expression in bacterial cells is tightly regulated at the transcriptional level by the repressor protein TtgR. In the absence of inducer molecules, TtgR binds to a specific operator DNA site and blocks the transcription of the ttgABC operon. However, the presence of antimicrobial compounds triggers the dissociation of TtgR from the operator site and subsequently activates the expression of the TtgABC efflux pump.[10] The transcriptional regulator TtgR thus plays an essential role in mediating the resistance level of *P. putida* DOT-T1E. An understanding of how TtgR interacts with substrates at the molecular level provides valuable insights into the complex regulatory mechanisms underlying antimicrobial resistance in bacteria.

TtgR belongs to the tetracycline repressor (TetR) family of transcriptional regulators and adopts a homodimeric struc-ture.[11] As depicted in Figure 1, each monomer of TtgR comprises nine α-helices that form an N-terminal DNA binding domain and a C-terminal ligand binding domain. The two domains are positioned at an angle of approximately 80° relative to each other. The ligand binding pocket of TtgR is formed by residues from five helices and features two distinct regions.[12] The upper and side walls of the pocket are primarily composed of hydrophobic residues, including Leu92, Leu93, Val96, Ile141, and Phe168. Conversely, the bottom of the pocket consists mainly of hydrophilic residues such as Asn110, His114, and Asp172. This combination of hydrophobic and hydrophilic binding sites enables TtgR to interact with a variety of structurally unrelated antimicrobial compounds, contributing to its broad substrate specificity.[12]

The TtgR transcriptional regulator exhibits a notable affinity for flavonoids, which are abundant in fruits, vegetables, and flowers and renowned for their antiviral and antibacterial properties.[14−17] As demonstrated in Figure 2, flavonoids possess polyphenolic structures and share a basic skeleton consisting of two benzene rings (A and B) connected by a
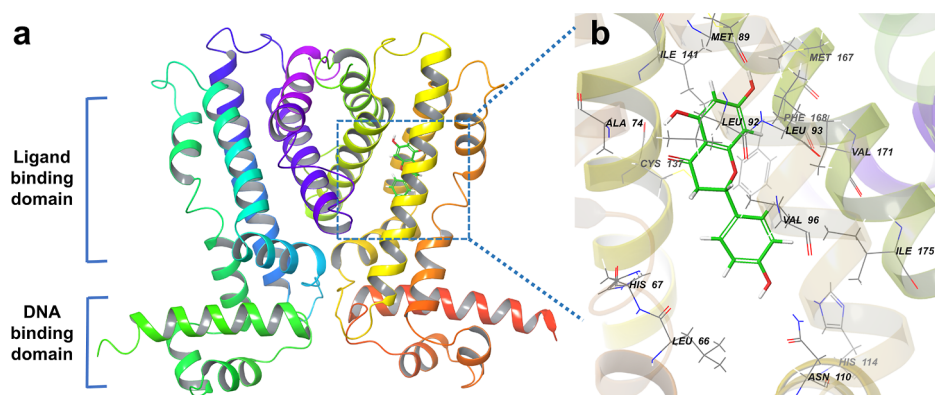
Figure 1. (a) Crystal structure of TtgR with naringenin bound in the active site (PDB ID 2UXU).[12] The 18 α-helices are represented in different colors. (b) Ligand binding pocket of TtgR with naringenin bound. Gray, red, blue, and white represent C, O, N, and H atoms, respectively. C atoms in naringenin are highlighted in lime. Graphics are generated using the Schrödinger Maestro software.[13]
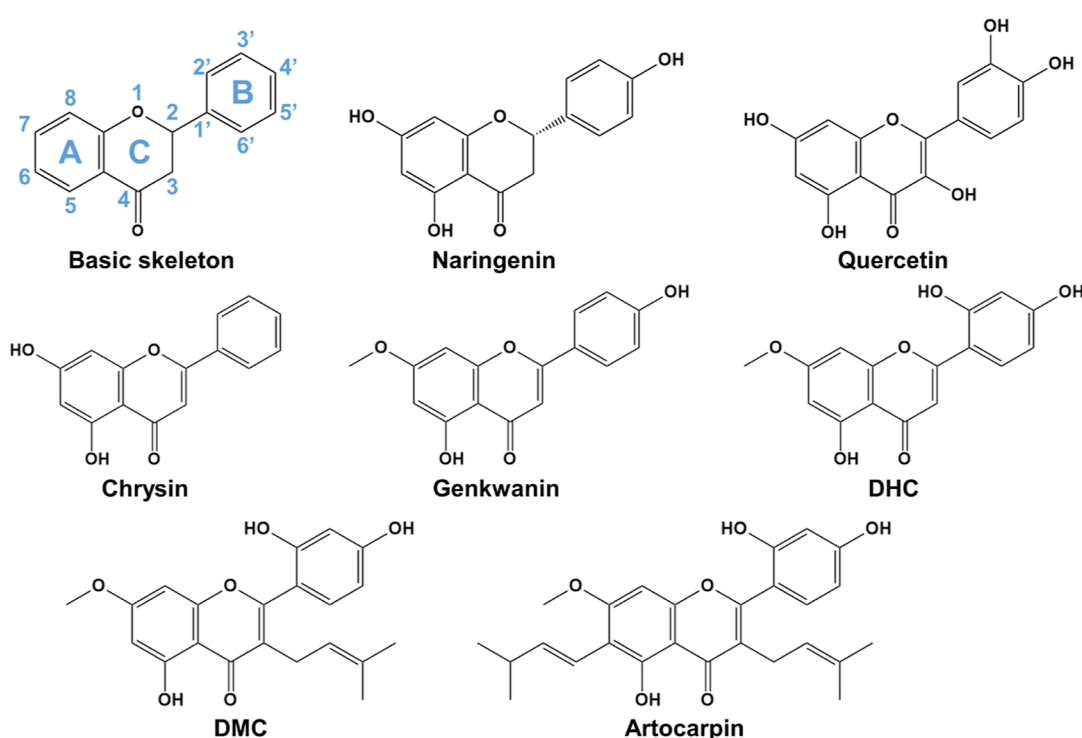

Figure 2. Skeleton representation of flavonoids and chemical structures of the seven flavonoids studied in this work. The rings are labeled and each ring atom is numbered in the skeleton structure.

heterocyclic ring C, forming a C6−C3−C6 configuration. These plant secondary metabolites adopt a wide range of chemical compositions and molecular geometries. They are categorized into subgroups such as flavonols, flavones, flavanones, anthocyanidins, chalcones, and isoflavones based on the degree of unsaturation and oxidation of ring C and the substitution patterns in rings A and B.[15] For example, naringenin is a flavanone characterized by a single bond between the C2 and C3 atoms and a C4═O group on ring C. In comparison, quercetin is a flavonol featuring a C2═C3 double bond, a C4═O group and a 3-OH group on ring C (Figure 2).

X-ray diffraction studies have revealed that TtgR binds to naringenin, quercetin, and phloretin by enveloping their fused rings A and C with hydrophobic residues near the top of the ligand binding pocket. Simultaneously, ring B establishes hydrogen bonding interactions with hydrophilic residues

located at the bottom of the active site (Figure 1).[12] These specific protein−ligand interactions contribute to the high susceptibility of *P. putida* DOT-T1E to these flavonoids.[7] Isothermal titration calorimetry experiments have further shown that ligand binding in TtgR is driven by favorable enthalpy changes, with quercetin and phloretin exhibiting stronger affinity for the protein compared to naringenin and other plant antimicrobials.[7] Despite these intriguing findings, comprehensive biochemical and structural biology assessment of flavonoids binding in the active site of TtgR remain limited. Given the potent antimicrobial activity that many flavonoids display against both Gram-positive and Gram-negative bacteria,[16,17] it is desirable to conduct extensive evaluations of their interactions with the TtgR transcriptional regulator.

Complementary to experimental investigations, the TtgR transcriptional regulator has garnered considerable attention in computational studies.[18−22] Recently, Zhang and co-workers
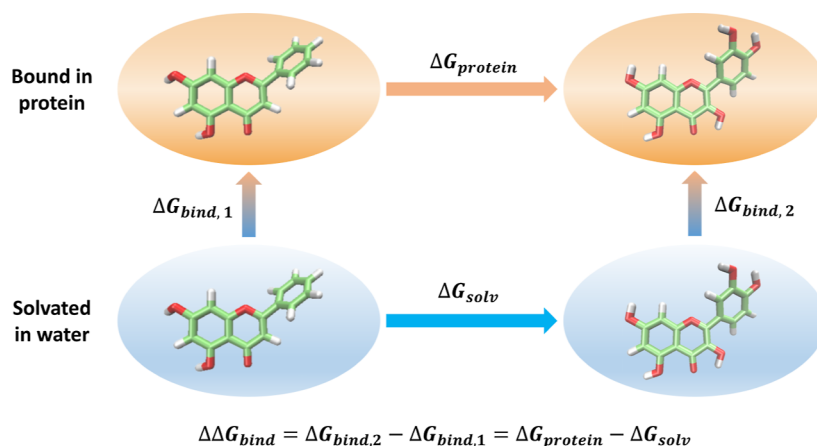
Figure 3. Thermodynamic cycle used in the calculation of relative binding free energies between two ligands. The transformation from chrysin to quercetin is shown as an example. Lime, red, and white represent the C, O, and H atoms, respectively, and the blue and orange backgrounds represent the aqueous and protein environments, respectively. $\Delta G_{bind,i}$ is the absolute binding free energy of ligand i, and $\Delta\Delta G_{bind}$ is the relative binding free energy between the two ligands. ΔG_{solv} and $\Delta G_{protein}$ are the changes in free energy when ligand 1 is transitioned into ligand 2 in the aqueous and protein environments, respectively.

performed equilibrium and nonequilibrium free energy simulations to predict the binding thermodynamics of TtgR toward a series of organic molecules and drugs, and examined the dynamics of the resulting protein−ligand complexes.[19] Considering the significant antimicrobial potential of flavonoids, in this work, we focus on seven such compounds and their derivatives and utilize a combination of molecular dynamics (MD) and alchemical free energy (AFE) simulations to explore their binding free energies and modes of interactions with the TtgR transcriptional regulator. As illustrated in Figure 2, these molecules comprise naringenin, quercetin, chrysin, genkwanin, artocarpin, 2-(2,4-dihydroxyphenyl)-5-hydroxy-7-methoxy-chromen-4-one (DHC) and 2-(2,4-dihydroxyphenyl)-5-hydroxy-7-methoxy-3-(3-methylbut-2-enyl)chromen-4-one (DMC). Beyond naringenin and quercetin, chrysin, genkwanin, and artocarpin belong to the flavone subgroup, representing naturally occurring flavonoids with well-established antimicrobial activities.[16,23] DHC and DMC serve as intermediate structures for the free energy calculations. The seven compounds exhibit notable variations in the degrees of saturation and substitution patterns in rings A, B, and C. Our simulations will reveal the influences of these structural elements on the binding geometries, affinities, and dynamics of the ligands in TtgR, thereby providing molecular insights into potential pharmaceutical applications of the flavonoids.

■ COMPUTATIONAL METHODS

MD Simulations. To set up the MD simulations, we obtained the TtgR-naringenin and TtgR-quercetin complexes from the Protein Data Bank (PDB IDs 2UXUand2UXH).[12] For the other flavonoids, we optimized their geometries in vacuum with the B3LYP density functional[24,25] and the 6-31G* basis set using the Gaussian 16 package.[26] The optimized structures were then placed in the active site of TtgR employing the AutoDock Vina program with the flexible ligand docking method and the united-atom scoring function.[27] To comprehensively cover the binding pocket of TtgR, a grid configuration of 38 × 36 × 34 with a grid interval of 0.375 Å was used along the x, y and z directions.

MD simulations of the protein−ligand complexes were performed using the Amber 2016 package.[28,29] Although it is

not the latest version, Amber 2016 provides all the necessary functions for standard MD simulations. TtgR and the flavonoids were modeled with the Amber ff14SB and the general amber force fields, respectively.[30,31] Water molecules were described using the TIP3P model.[32] In each system, the protein−ligand complex was solvated in an octahedral water box with a minimal distance of 12 Å to any edge of the box, and 14 Na$^+$ ions were added to neutralize the charges. The system underwent a two-step energy minimization. First, the coordinates of the protein−ligand complex were held fixed while the ions and water molecules were allowed to move and adjust their positions. In the second minimization step, only the ligand was subject to position restraints. Following energy minimization, restrained equilibration was conducted in the *NVT* and *NPT* ensemble, each for 1 ns. Restraining forces were applied to the non-H atoms in the protein−ligand complexes using a force constant of 5.0 kcal/mol/Å^2. Position restraints were then relaxed and the systems were equilibrated under the *NPT* condition for 2 ns. Production runs extended for 20 ns in the *NPT* ensemble and the trajectories were saved every 0.05 ps for further analysis. The simulations were performed with a time step of 2 fs. The simulation temperature was maintained at 300 K using the Langevin thermostat,[33] and the pressure was kept at 1 atm using the Berendsen barostat.[34] Lennard-Jones interactions were calculated with a cutoff of 12 Å, and long-range electrostatic interactions were treated using the particle-mesh Ewald method.[35] The LINCS algorithm was applied to constrain H-containing chemical bonds in the systems.[36]

From the simulations, we analyzed the hydrogen bonds formed between the flavonoids and the active-site residues of TtgR. A hydrogen bond was considered to be present if the donor (D) and acceptor (A) atoms were O or N, the D−A distance ≤3.0 Å, and the D−H−A angle ≥135°.[29] Representative configurations were extracted from the MD simulations, and their corresponding interaction maps were generated using the Schrödinger Maestro software.[13] Additional analyses are provided in the Supporting Information.

AFE Simulations. AFE simulations have been used extensively in drug discovery for the prediction of ligand−protein binding, and have been the subject of several reviews.[37−49] We conducted AFE simulations to compute the

relative binding free energies of the flavonoids using the Amber 2022 package[50] and AMBER Drug Discovery Boost Tools[51] that leverage high-performance GPU acceleration.[52,53] The version differences in the Amber program for standard MD simulations and AFE simulations are expected to have minimal impact on the prediction results. The relative binding free energy between ligands 1 and 2 in TtgR is defined as the difference between their absolute binding free energies, $\Delta\Delta G_{bind} = \Delta G_{bind,2} - \Delta G_{bind,1}$. Given the challenges associated with obtaining absolute binding free energies along a specific physical pathway, we applied a thermodynamic cycle (Figure 3) to calculate $\Delta\Delta G_{bind}$. Leveraging the fact that Gibbs free energies are state functions, we establish the relationship $\Delta G_{bind,2} - \Delta G_{bind,1} = \Delta G_{protein} - \Delta G_{solv}$, where $\Delta G_{protein}$ and ΔG_{solv} represent the changes in free energy when ligand 1 is transformed into ligand 2 through an alchemical pathway in a protein or aqueous environment, respectively.

The transformation between two flavonoids is performed through a series of intermediate states characterized by a coupling parameter, λ. By varying λ from 0 to 1, the system gradually transitions from ligand 1 to ligand 2, and $\Delta G_{protein}$ and ΔG_{solv} are calculated using a thermodynamic integration (TI) free energy formulation[54,55]

$$\Delta G_i = \int_0^1 \langle \frac{\partial U_i(\lambda)}{\partial \lambda} \rangle_\lambda d\lambda \tag{1}$$

Here, $U_i(\lambda)$ is the λ-coupled potential function that "alchemically" transforms ligand 1 into ligand 2 in either the protein or aqueous environment. In the AFE simulations using Amber,[45] the transforming region is separated into two parts: (1) a "common core" where there is a one-to-one mapping of atoms of ligand 1 as they transform into those of ligand 2 by changing force field parameters and (2) a "softcore" region where there is no such one-to-one mapping and the coordinates of the atoms of the two ligands are separable and the interactions with the environment are "softened" by using so-called "softcore" potentials[56,57] that remove singularities at the origin that may cause numerical instabilities. The robustness and precision of the AFE calculations depend intimately on the atom mapping procedure that establishes the magnitude of the perturbation, together with the form of the alchemical transformation pathway and method for enhancing the phase space sampling used to achieve convergence of the numerical averages.[45] In the current work, the extended maximum common substructure network (MCS$-$E$_{nw}$) algorithm was applied to automatically identify the common core and softcore regions for each transformation.[58] The production runs utilized the recently developed optimized alchemical pathways that employ a modified second-order smoothstep softcore potential[56] and concerted "single-step" transformation described in detail elsewhere.[57] An alchemical enhanced sampling (ACES) approach[59] implemented in the Amber software was used to streamline phase space sampling and improve the precision of the AFE calculations.

For each alchemical transformation, the protein and ligands were modeled using the AMBER ff14SB and the GAFF2 force fields,[30,60] respectively, and the explicit water model TIP4P/Ew was chosen with the corresponding Joung$-$Cheatham Na$^+$ and Cl$^-$ ion parameters.[61] Each protein$-$ligand complex was solvated in a cubic box containing 24,958 water molecules, and 82 Na$^+$ and 68 Cl$^-$ were added to reach an approximate physiological (extracellular) bulk concentration of 0.15 M. For the solution simulations, each ligand was surrounded by 3985

water molecules, along with 11 Na$^+$ and 11 Cl$^-$ ions. We conducted a series of minimization and equilibration steps for both the $\lambda = 0$ and $\lambda = 1$ states. First, non-H atoms in the flavonoids or TtgR-flavonoid complexes were fixed at their initial positions, allowing ions and water molecules to relax in the energy minimization process. Position restraints were applied with a force constant of 5 kcal/mol/Å^2. A second minimization was performed without position restraints. Subsequently, equilibration in the NPT ensemble was conducted for 0.5 ns at a temperature of 300 K and pressure of 1 atm, while the non-H atoms in the solute were restrained. The box dimensions were determined by averaging the values from the $\lambda = 0$ and $\lambda = 1$ states. MD simulations were then carried out under the NVT condition for 0.5 ns for both states, generating all intermediate replicas with the same box shape. The system was then heated at a constant volume to 300 K for an additional 0.5 ns. An NPT equilibration was performed for 0.5 ns, followed by a 2 ns annealing process. During annealing, the system was heated to 600 K in the first 50 ps, maintained at 600 K for 100 ps, and cooled down to 300 K for 50 ps. After annealing, restraints on the solute atoms were gradually reduced to zero in the following steps over 1.2 ns: force constant of 2 kcal/mol/Å^2 for 200 ps, 1 kcal/mol/Å^2 for 200 ps, 0.5 kcal/mol/Å^2 for 200 ps, 0.25 kcal/mol/Å^2 for 200 ps, 0.1 kcal/mol/Å^2 for 200 ps, and no restraints for the final 200 ps.

We generated $\lambda \leq 0.5$ windows from the $\lambda = 0$ state and the $\lambda > 0.5$ windows from the $\lambda = 1$ state, resulting in a total of 21 windows. Each λ window underwent 5000 steps of energy minimization using the steepest descent method, and a 0.5 ns equilibration in the NPT ensemble. The system was then heated to 300 K within 300 ps, followed by a 2 ns equilibration. Production runs in the NPT ensemble were performed for 5 ns using the ACES method.[59] A time step of 1 fs was used for all the AFE simulations. In the simulations, the temperature was maintained at 300 K using the Langevin thermostat,[33] and the pressure was kept at 1 atm using the Monte Carlo barostat.[62] Hamiltonian replica exchange was invoked to enhance system sampling, exchanging coordinates and velocities between two neighboring λ windows every 20 fs. The first 0.5 ns of the trajectories were discarded for equilibration, and the remaining data were used for production analysis. The analysis was conducted using the edgembar module from AmberTools23,[63] and free energies were calculated using both the multistate Bennett's acceptance ratio (MBAR) and TI methods.[45,64,65] In no cases were there statistically significant differences between the MBAR and TI free energy estimates for the systems studied in the present work, although they were nonetheless compared as a consistency test. Given the similarity between the predicted free energies from the two methods, we presented only the MBAR results in the subsequent analysis. Standard errors for the average $\Delta\Delta G_{bind}$ values were estimated from bootstrapping analysis that included consideration of statistical inefficiencies of correlated time series data from individual simulations, as well as variances between three independent trials where simulations were repeated with different random number seeds. Detailed statistical errors for individual trials for all simulations are provided in Table S1 of the Supporting Information.

Table 1. Chemical Features and $\Delta\Delta G_{bind}$ of the Seven Flavonoids and Their Derivatives in the TtgR Transcriptional Regulator[a]

flavonoid	chrysin	naringenin	quercetin	genkwanin	DHC	DMC	artocarpin
C2−C3 bond type	double	single	double	double	double	double	double
3-substituent			−OH			−CH$_2$CH=C(CH$_3$)$_2$	−CH$_2$CH=C(CH$_3$)$_2$
6-substituent							−CH=CHCH(CH$_3$)$_2$
7-substituent	−OH	−OH	−OH	−CH$_3$O	−CH$_3$O	−CH$_3$O	−CH$_3$O
2′-OH					√	√	√
3′-OH			√				
4′-OH		√	√	√	√	√	√
$\Delta\Delta G_{bind}$ (kcal/mol)	0	−1.34	−1.70	−2.85	−4.23	−5.72	−7.32
standard error (kcal/mol)	0.09	0.16	0.08	0.07	0.07	0.09	0.11

[a]$\Delta\Delta G_{bind}$ are obtained from AFE simulations and the binding free energy of chrysin is taken as a reference.

■ RESULTS AND DISCUSSION

Relative Binding Free Energies of the Flavonoids. As depicted in Figure 2, the seven flavonoids and their derivatives share a common skeleton structure characterized by two fused rings A and C and a phenyl ring B connected by a C−C bond. Additionally, they feature a C4=O group on the heterocyclic ring C and a 5-OH group on ring A. Among these compounds, naringenin exhibits a unique configuration with a saturated ring C, where the C2−C3 single bond imparts a nonplanar ring geometry and introduces a chiral center to the molecule. It also possesses a 7-OH group on ring A and 4′-OH group on ring B. In contrast, the remaining molecules have C2=C3 double bonds and varying substituent groups at positions 3, 6, 7, 2′, 3′, and 4′ across the three rings. These differences in oxidation levels and substituents are summarized in Table 1.

We have conducted AFE simulations in aqueous solutions and TtgR-ligand complexes to calculate the relative binding free energies of the seven flavonoids. Among the recent advancements in AFE methods,[40−49] we have invoked the ACES approach to enhance conformational and alchemical sampling and produce reliable free energy estimates.[59] As illustrated in Figure 4, the common cores incorporate the basic skeleton of the flavonoids, while the softcore regions undergo transformation between two ligands in each AFE simulation. For example, in the alchemical transformation from chrysin to quercetin, substituent groups at positions 3, 3′ and 4′ of rings B and C are designated as softcore atoms. The chemical bonds and angles involving these atoms as well as dihedral angles connecting the common cores and softcores are scaled by the λ parameter in the AFE simulations. In the conversion from chrysin to naringenin, which differs considerably in bond saturation and planarity of ring C, the softcore region encompasses the entire ring B, its substituent group, and the C2−C3 bond. Notably, substantial structural differences between quercetin and artocarpin prevent AFE simulations from providing accurate predictions of free energies (Figure S2). To address this issue, we introduce three intermediate structures, genkwanin, DHC, and DMC, to facilitate the gradual conversion between the two flavones and enable the determination of their differences in binding free energies.

We apply a variety of metrics to evaluate the convergence of the AFE simulations as implemented in the FE-ToolKit analysis package available in AmberTools.[63] First, we perform forward and reverse time-series simulations to derive the alternations in free energy as a function of sampling fraction.[66] Using the transformation from chrysin to naringenin as an example, Figure 5a demonstrates that $\Delta G_{protein}$ from the forward and reverse analyses converges to within the standard error margin after the initial 10% sampling fraction, yielding a consistent value of −53.82 kcal/mol. Second, the smooth variation of the $\left\langle \frac{\partial U}{\partial \lambda} \right\rangle$ value across all λ windows, as depicted in Figure 5b, confirms the convergence in the AFE calculations. Additionally, we compute the free energy changes from both MBAR and TI methods and compare their results. TI with trapezoidal-rule integration generates a free energy of −53.84 kcal/mol with a standard error of 0.09 kcal/mol, while MBAR provides an estimate of −53.82 ± 0.07 kcal/mol. The difference between their predictions falls within the statistical error bounds, indicating the convergence and stability of the AFE simulations.[67] Finally, based on Table S6, the phase space overlaps between neighboring λ states all exceed 0.42 and are sufficient to ensure a reliable free energy prediction.[45]

From the AFE simulations, the seven flavonoids exhibit a broad range of 7.32 kcal/mol in their $\Delta\Delta G_{bind}$ values (Table 1). The standard errors associated with the free energy analysis are within 0.16 kcal/mol. Chrysin, characterized by its structural simplicity, shows the weakest interaction with TtgR and is taken as the reference for the binding free energies. Naringenin possesses a nonplanar ring C geometry and similarly demonstrates a modest binding affinity with $\Delta\Delta G_{bind}$ of −1.34 kcal/mol. Notably, $\Delta\Delta G_{bind}$ increases with structural complexity and the presence of substituent groups, with artocarpin emerging as the most potent binder. Our observation that the $\Delta\Delta G_{bind}$ value of quercetin is 0.36 kcal/mol lower than that of naringenin aligns closely with recent isothermal titration calorimetry experiments, which reports a free energy difference of 0.39 ± 0.02 kcal/mol between the two compounds.[7] To elucidate the origin of the diverse binding affinities, we will explore the interaction patterns of the flavonoids in the TtgR binding site.

Molecular Interactions between Flavonoids and the TtgR Transcriptional Regulator. Throughout the MD simulations, the flavonoids and their derivatives remain bound in the active site of the TtgR transcriptional regulator. Their binding poses, as demonstrated in Figures 6 and 7, exhibit varying orientations depending on the types and positions of the substituent groups as well as the size and shape of the molecules. Chrysin, naringenin, quercetin, genkwanin, DMC, and artocarpin are positioned consistently with rings A and C occupying the upper region of the binding pocket. The fused rings form stabilizing van der Waals interactions with a cluster of hydrophobic residues, including Met89, Leu92, Leu93, Val96, and Ile141. Note that chrysin possesses the smallest molecular structure and displays the most flexible binding configuration, directing its fused rings in the opposite
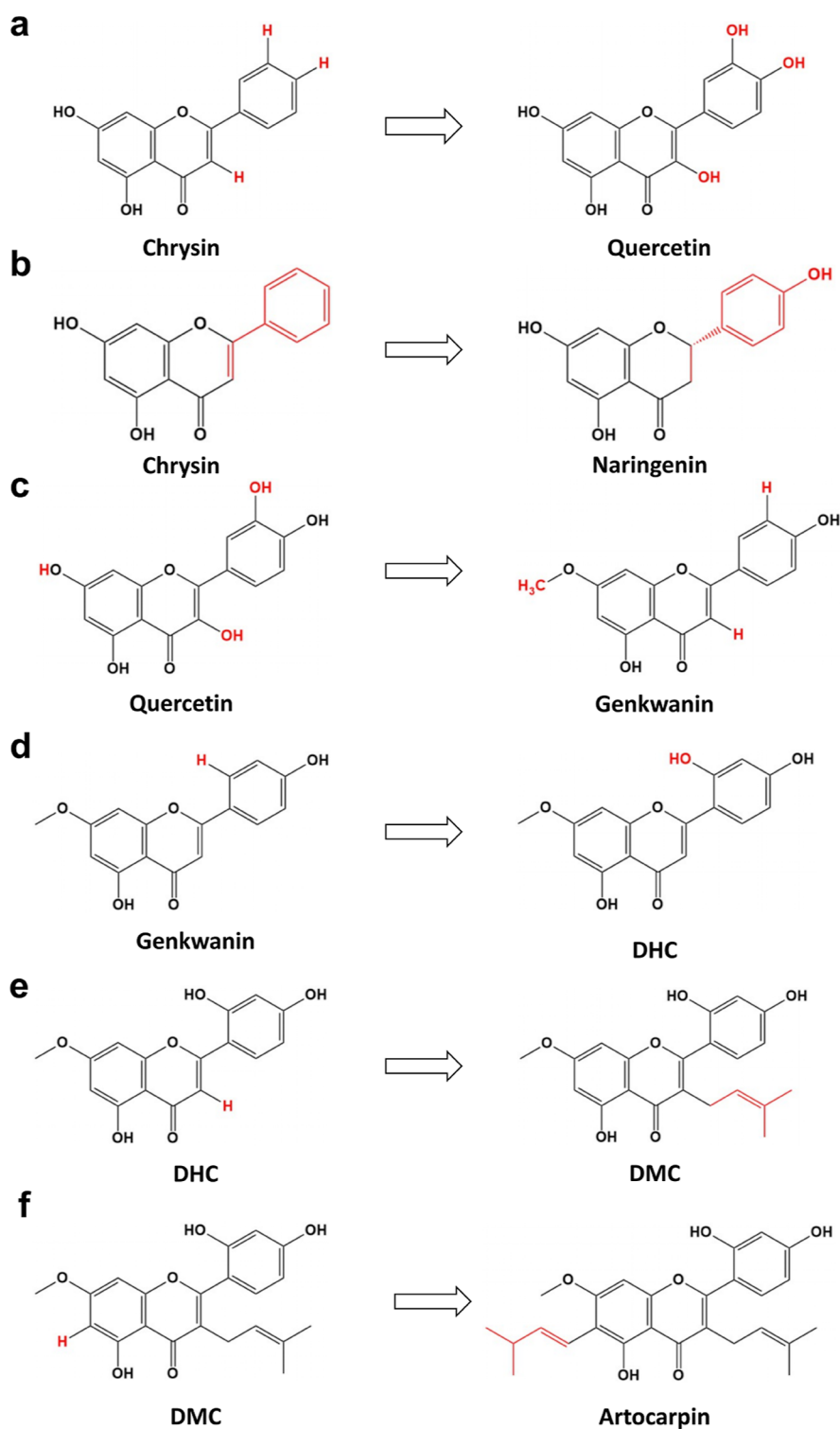
Figure 4. Illustrations of the common core and softcore regions in the AFE simulations. The softcore atoms for each transformation are highlighted in red.

direction compared to the other flavonoids. Across all systems, ring B assumes an almost perpendicular orientation relative to the rest of the molecule, pointing toward the bottom of the binding pocket. Furthermore, the O-containing functional groups on the rings establish electrostatic and hydrogen bonding interactions with polar and charged amino acid residues such as His70, Asn110, and Asp136. In contrast to the other ligands, DHC adopts a distinct binding pose

characterized by a nearly horizontal alignment within the active site of TtgR (Figure 7b). This unique spatial arrangement is stabilized through a combination of van der Waals, electrostatic, and hydrogen bonding interactions with residues situated in the side walls of the binding pocket.

Analysis of π−π and CH/π Interactions. From Figures 6 and 7, the flavonoids possess a variety of functional groups that participate in intricate interactions with the active-site residues
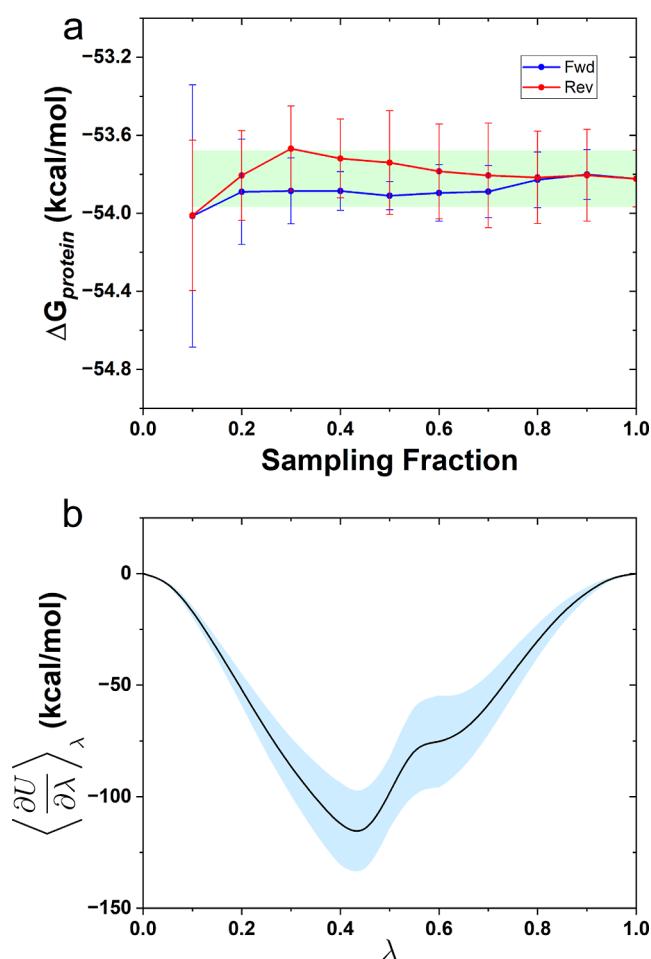
Figure 5. Convergence performance of the AFE simulations during the transformation from chrysin to naringenin in the protein−ligand complex. (a) Comparison of $\Delta G_{\text{protein}}$ from forward and reverse AFE simulations at different sampling percentages, averaged over three independent trials. The light green band represents the final $\Delta G_{\text{protein}}$ within the standard error. (b) Variation of $\langle \frac{\partial U}{\partial \lambda} \rangle_\lambda$ at different λ values. The black line represents cubic spline interpolation, and the light blue region indicates the standard deviation.

of TtgR. To dissect these intermolecular forces, we start by examining the aromatic moieties in the molecular structures. We first consider their $\pi−\pi$ interactions with residues containing aromatic side chains, namely His67, His70, His114, and Phe168, in the binding pocket. Surprisingly, while quercetin, DMC, and artocarpin are observed to stack with the aromatic residues, these $\pi−\pi$ interactions are relatively weak with stacking distances and angles varying over a broad range (Figure S1).

We then explore potential CH/π hydrogen bonds formed between the π-electrons in ring A or B of the ligands and the −CH, −CH$_2$, and −CH$_3$ groups in the side chains of surrounding hydrophobic residues. Although classical force fields are not parametrized to accurately characterize these weak non-bonded interactions, they have been shown to provide qualitatively correct predictions of the presence and interaction energies of CH/π hydrogen bonds.[68] To characterize them in the active site of TtgR, we calculate the distance between the center of mass of ring A or B of a flavonoid (denoted as X) and the C atom in a side-chain alkyl group,

d_{CX}, and the C−H−X angle, α, for each interaction pair. The free energies are then obtained as

$$F = -k_{\text{B}}T \ln P(d_{\text{CX}}, \alpha) \tag{2}$$

Here, k_{B} is the Boltzmann constant, T is the simulation absolute temperature, and $P(d_{\text{CX}}, \alpha)$ represents the probability of observing a flavonoid ring in a specific configuration (d_{CX}, α) relative to the alkyl side chain of an amino acid. As shown in Figure 8, d_{CX} predominantly falls within the range of 3 to 5 Å, while α spans from 90 to 180° for the binding of the seven flavonoids. For chrysin, naringenin, quercetin, and genkwanin, ring A closely interacts with the side-chain alkyl groups of the active-site residues, with their most stable configurations characterized by d_{CX} below 4 Å and α exceeding 115°. Conversely, for DMC and artocarpin, ring B is in close proximity to the hydrophobic side chains and their most favorable configurations occur at d_{CX} of 3−4.5 Å and $\alpha \sim 120°$. These geometric parameters suggest the presence of prevalent CH/π hydrogen bonds[69] between the flavonoids and the active-site residues in TtgR, particularly Leu93, Val96, and Ile141. This observation is consistent with recent studies conducted by Zhang and co-workers, who identified $\pi−$alkyl interactions are important stabilizing forces in the binding of quercetin to TtgR.[19] Among the seven ligands, DHC exhibits the weakest CH/π interactions as the most stable binding configuration of its aromatic rings occurs at $d > 6$ Å and $\alpha > 120°$. Both parameters display a broad range of variations, reflecting its unique horizontal binding pose in the protein.

Influence of Substituent Groups on Flavonoid Binding. Next, we analyze the influences of substituent groups on the binding of flavonoids in TtgR. Using chrysin as a reference, two major substituent patterns emerge: hydroxyl groups on ring B and alkyl groups on the fused rings A and C (Figure 2). Naringenin and quercetin offer valuable insights into the effects of hydroxyl groups. From Figure 6b, the presence of a 4′-OH group allows ring B of naringenin to penetrate deeper into the binding pocket, forming a hydrogen bond with the side chain amide group of Asn110. Although this hydrogen bond persists for only 39.7% of the MD simulations (Table S2) due to naringenin's structural flexibility introduced by the nonplanar ring C configuration, it contributes to the stabilization of the molecule and results in a $\Delta\Delta G_{\text{bind}}$ of −1.34 kcal/mol compared to chrysin. In contrast, quercetin features a C2=C3 double bond and three hydroxyl groups at positions 3, 3′ and 4′ of rings B and C. With the planar geometry of its fused rings, quercetin experiences reduced steric hindrance and assumes a more vertical orientation in the binding pocket (Figure 6c). Its 4′-OH group forms a relatively stable hydrogen bond with the carboxylate side chain of Asp172, existing in 48.5% of the MD trajectories. Additionally, the 3′- and 4′-OH groups occasionally participate in hydrogen bonding interactions with the side chains of Asn110 and His114, respectively (Table S2). Interestingly, the 3-OH group is highly solvent exposed and interacts with 14 water molecules from the MD trajectory. These hydroxyl substituents enhance favorable protein−ligand interactions, consistent with previous observations in X-ray diffraction experiments that quercetin shows stronger electron densities in the hydroxyphenyl ring compared to naringenin.[12] Accordingly, quercetin exhibits tighter binding with TtgR than chrysin and naringenin with a $\Delta\Delta G_{\text{bind}}$ value of −1.70 kcal/mol.

Similarly, genkwanin, DMC, and artocarpin contain 1 or 2 hydroxyl groups at positions 2′ and 4′ of ring B. As depicted in
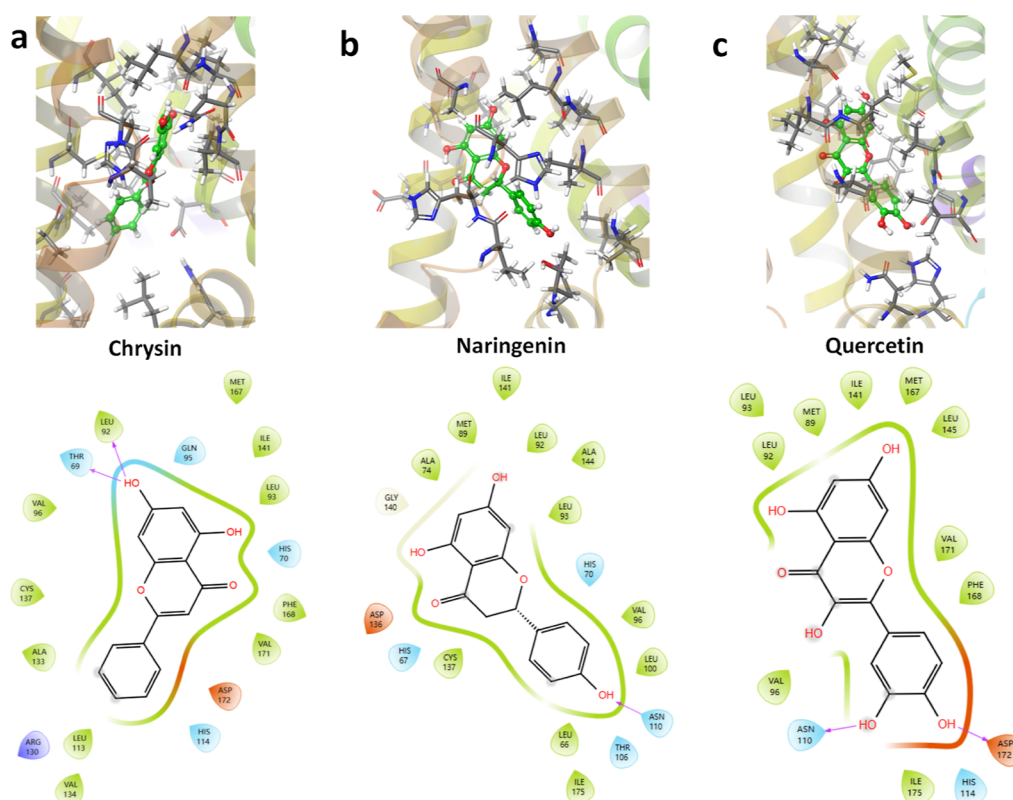
Figure 6. Representative structures and interaction maps for the binding of (a) chrysin, (b) naringenin, and (c) quercetin in the TtgR transcriptional regulator. In the protein−ligand complexes, gray, red, blue, and white represent C, O, N, and H atoms, respectively, and lime represents C atoms in the flavonoids. In the interaction maps, the green, blue, orange, and purple bubbles represent hydrophobic, polar, negatively charged, and positively charged residues, respectively. Pink arrows indicate hydrogen bonding interactions and atoms with a gray shadow are solvent exposed.

Figure 7, these compounds assume a vertical orientation in the TtgR binding pocket with the 4′-OH group forming hydrogen bonds with the amide O and N atoms of the Asn110 side chain. For genkwanin, the 4′-OH group extends its hydrogen bonding network to include the side chain of Asp172, establishing connections either directly or via a bridging water molecule. In the case of DMC, the additional 2′-OH group fosters hydrogen bonds with the side chain hydroxyl group of Thr69 and the backbone carbonyl group of Leu66 (Table S2). Beyond the hydroxyl moieties, these compounds feature nonpolar substituent groups on the fused rings A and C. Notably, artocarpin has 3-methylbut-2-enyl, 3-methylbut-1-enyl and methoxy substituent groups at positions 3, 6 and 7, respectively. The combination of polar and nonpolar functional groups in artocarpin enhances its van der Waals interactions with nonpolar residues such as Ala74, Leu92, Leu113, Leu143, Ala144, and Phe168 at the top and side walls of the binding pocket (Figure 7d). Consequently, artocarpin shows the strongest binding affinity toward TtgR with a $\Delta\Delta G_{bind}$ value of −7.32 kcal/mol.

Nature of Key Molecular Interactions between Flavonoids and TtgR. The above analysis suggests that TtgR transcription regulator uses a network of noncovalent interactions to bind and recognize flavonoids. For the seven compounds, the fused rings A and C reside near the top of the binding cavity and are primarily stabilized through van der Waals interactions, CH/π hydrogen bonding and $\pi-\pi$ stacking with the surrounding hydrophobic residues. Introducing nonpolar substituents to the fused rings enhances these interactions and contributes to

ligand stabilization. Depending on the molecular size and shape, the flavonoids exhibit various orientations of ring B in the TtgR active site. Naringenin, quercetin, genkwanin, DMC, and artocarpin preferably adopt a nearly vertical orientation, directing the hydroxyl groups of ring B toward the bottom of the active site. Given the abundant hydrophilic residues in the lower side of the binding pocket, electrostatic, and hydrogen bonding interactions become essential for ligand stabilization. Concurrently, water molecules are present, forming direct hydrogen bonds to flavonoids or acting as hydrogen bonding bridges to connect their hydroxyl groups and the hydrophilic active-site residues. In contrast, DHC lies almost horizontally with its 2′- and 4′-OH groups involved in hydrogen bonding interactions with residues at the side wall of the binding pocket.

Flavonoids with a saturated ring C, such as naringenin, experience considerable steric hindrance that prevents their hydroxyl groups from reaching deeply buried residues and form stable hydrogen bonds in the binding pocket of TtgR. As a result, flavonoids with a planar configuration of fused rings and a substantial number of hydroxyl substituents on ring B tend to exhibit higher binding affinities. Among the seven molecules studied, artocarpin is the most potent binder as its molecular geometry and substituent groups facilitate a wide arrange of favorable interactions with TtgR. From Table 1, the predicted $\Delta\Delta G_{bind}$ of artocarpin is 6 kcal/mol lower than that of naringenin. Based on previous thermodynamic measurements of naringenin,[7] this significant free energy difference suggests that artocarpin could be a subnanomolar binder of
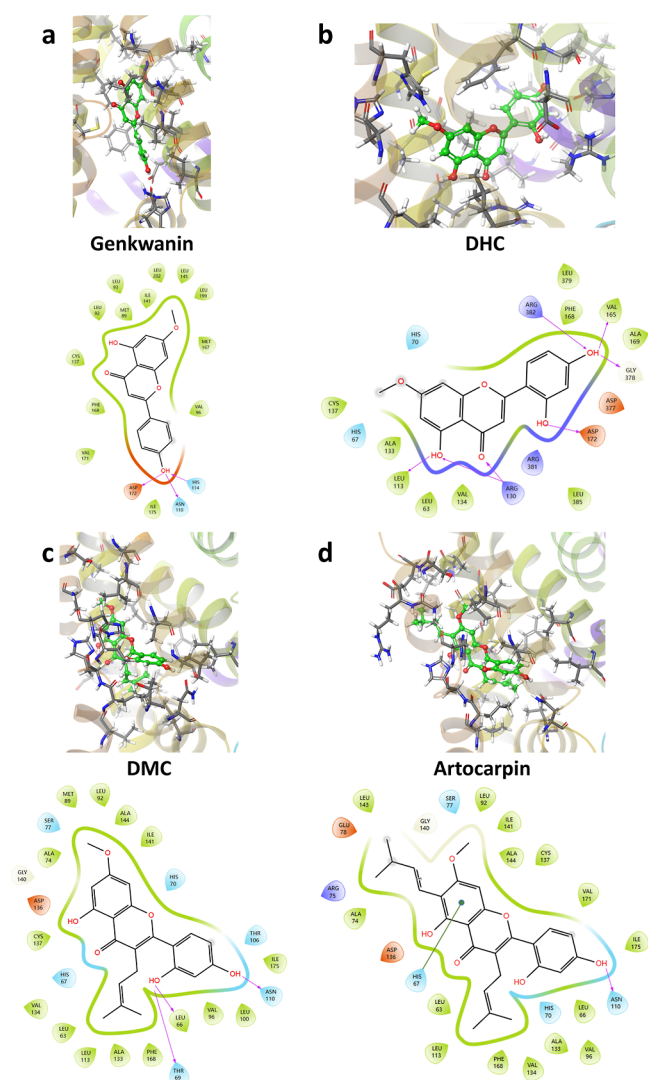
Figure 7. Representative structures and interaction maps for the binding of (a) genkwanin, (b) DHC, (c) DMC, and (d) artocarpin in the TtgR transcriptional regulator. Pink and blue arrows in the interaction maps indicate hydrogen bonding and π stacking interactions, respectively. The remaining color schemes are the same as those in Figure 6.

TtgR. This prediction could motivate new experimental investigations into the interactions of flavonoids with the

TtgR transcriptional regular, thereby validating our computational findings.

Confined Flavonoid Dynamics in the Active Site of TtgR. Given the intricate intermolecular interactions, it is expected that the flavonoids will display confined motion within the binding pocket of TtgR. Indeed, these compounds undergo jiggling motions within the active site, as indicated by their small self-diffusion coefficients that range between 0.8×10^{-11} and 1.9×10^{-11} m^2/s (Table S3). This sluggish translational motion aligns with the consistent binding observed for these ligands in the active site of TtgR throughout the MD simulations.

The aromatic moieties of flavonoids actively participate in CH/π hydrogen bonds and $\pi-\pi$ stacking interactions. Their rotational movements play crucial roles in the formation and disruption of these amino acid−ligand interactions. To examine the dynamics of these interactions, we analyze the aromatic rings A and B of the flavonoids and compute their rotational time correlation functions

$$R(t) = \langle P_2(\hat{n}_i(0)\cdot\hat{n}_i(t))\rangle \tag{3}$$

Here, P_2 is the second-order Legendre polynomial and $\hat{n}_i(t)$ denotes the unit vector of the surface normal of aromatic ring i in a flavonoid. As shown in Figure 9, the seven flavonoids exhibit constrained rotations within the active site of TtgR. Across all systems, $R(t)$ can be effectively characterized using a triexponential function. From Table S4, the rings display an initial fast decay with a time scale of approximately 1 ps, followed by an intermediate time scale ranging between 32 and 87 ps. For ring A of the flavonoids, a prolonged decay extending into the nanosecond range is observed, which arises from the favorable interactions between their π electrons and hydrophobic residues located at the top of the TtgR binding pocket. A similar slow long-time decay is observed for ring B of the flavonoids. However, in the cases of chrysin and genkwanin, ring B exhibits considerable rotational motion with decay constants of 310.2 and 425.0 ps, respectively (Table S4). This distinct behavior can be attributed to their small molecular size and reduced steric hindrance for the rotational movements within the bound complex.

Finally, we evaluate the hydrogen bonds formed between the hydroxyl groups on ring B of flavonoids and the active-site residues in TtgR. Except chrysin, all other flavonoids feature at least one hydroxyl group on ring B. Notably, the 4′-OH of naringenin, DMC, and artocarpin emerges as the primary
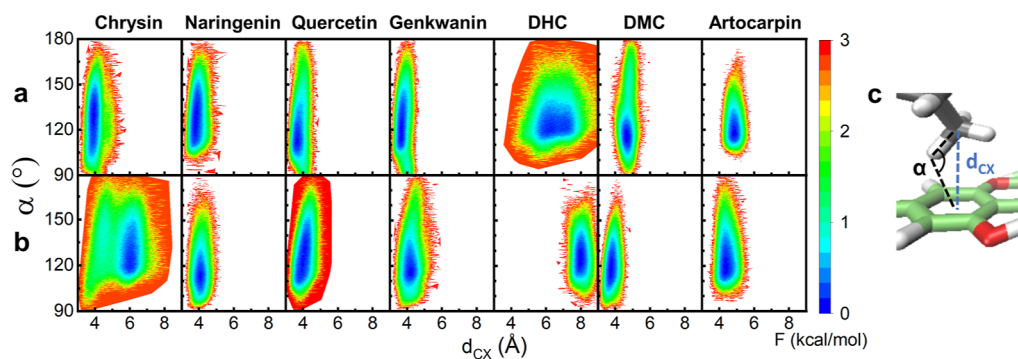

Figure 8. Two-dimensional free energy surfaces depicting the CH/π interactions between (a) ring A and (b) ring B of the flavonoids and the hydrophobic residues in the active site of TtgR. The free energies are shifted to set the minimal value at 0 in each plot. (c) Schematic representation of the d_{CX} and α parameters.
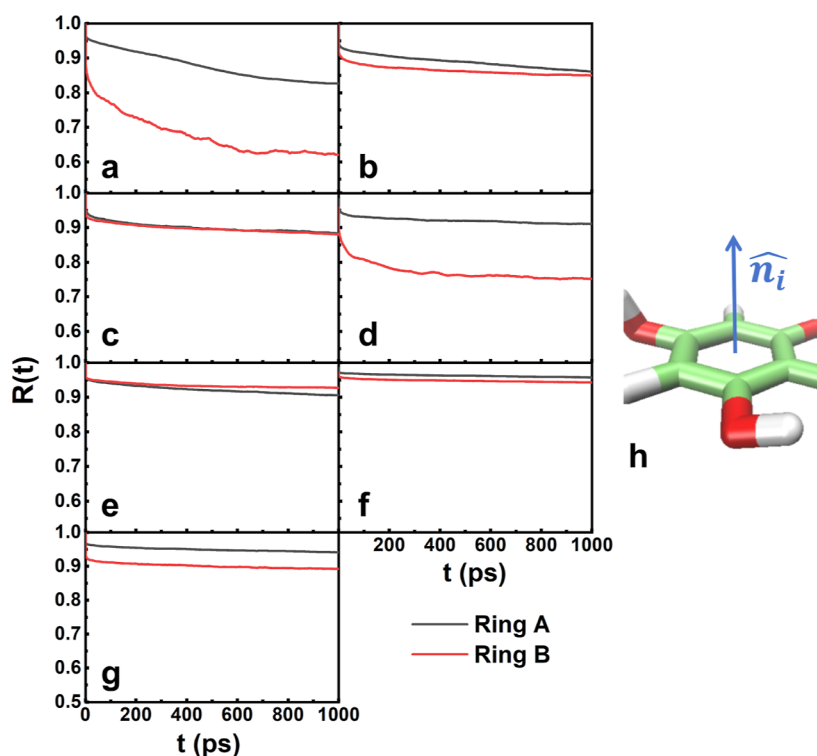
Figure 9. Normalized rotational time correlation functions for rings A and B of (a) chrysin, (b) naringenin, (c) quercetin, (d) genkwanin, (e) DHC, (f) DMC, and (g) artocarpin. The unit vector of the surface normal is illustrated in (h).

functional group that actively participates in hydrogen bonding interactions with the amide side chain of Asn110. Furthermore, the 4′-OH of quercetin and genkwanin and the 2′-OH of DHC establish hydrogen bonds with the carboxylate side chain of Asp172 (Table S2). To assess the dynamical properties of these hydrogen bonds, we compute their time correlation functions

$$C_{HB}(t) = \langle h(0)h(t) \rangle \qquad (4)$$

For a given flavonoid, the hydrogen bond status function, $h(t)$, assumes a value of 1 if the specified hydrogen bond is present and 0 if it is absent. As shown in Figure 10 and Table S5, DHC, DMC, and artocarpin, characterized by their larger molecular sizes and the concurrent presence of both 2′- and 4′-OH groups, exhibit minimal decay within 800 ps. This
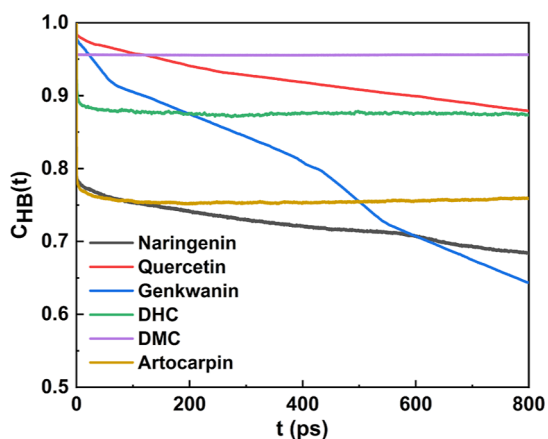
observation is consistent with the significant probabilities of 82.6, 95.6, and 75.5% for their hydroxyl groups to participate in hydrogen bonds, respectively, over the course of the MD simulations (Table S2). In contrast, naringenin shows a considerably faster but still sluggish long-term decay, with a time constant of 4010.1 ps (Table S5). This behavior is attributed to its nonplanar ring C structure and the presence of a chiral center at the C2 position. Accordingly, its 4′-OH group shows a significantly lower participation rate of 39.7% in hydrogen bonds with Asn110. A similar trend is observed for quercetin. Among the seven flavonoids, genkwanin displays the most rapid dynamics with a time constant of 2180.6 ps for the long-term decay of $C_{HB}(t)$. This aligns with the observation that its 4′-OH group has a low probability of 13.7% in forming hydrogen bonds with Asp172. Overall, all the seven flavonoids exhibit constrained dynamics in their hydrogen bonding interactions.

Conclusions. In this work, we combine MD and AFE simulations to reveal the geometries, relative free energies, and dynamics for the binding of seven flavonoids and their derivatives in the TtgR transcriptional regulator. The ligand binding pocket of TtgR is composed of two distinct regions: the upper side is mainly constituted of hydrophobic amino acids, while the lower side is enriched with polar residues. Through MD simulations, we observe that all of the flavonoids are anchored with their fused rings A and C near the top of the binding pocket. This binding pose is stabilized by a diverse range of noncovalent forces, including CH/π hydrogen bond, π–π stacking, and electrostatic interactions, with surrounding active-site residues. As a result, ring A exhibits restricted motions in both the translational and rotational degrees of freedom. In comparison, ring B of the flavonoids occupies a position closer to the bottom of the binding pocket, and its orientation and rotational dynamics are influenced by the size,

Figure 10. Normalized hydrogen bonding time correlation functions of the flavonoids.

planarity, and substituent groups of the molecule. Notably, the presence of hydroxyl substituents on ring B leads to direct hydrogen bonding interactions with deeply buried residues such as Asn110 and Asp172. These interactions significantly contribute to the overall stability of the protein−ligand complex and lead to constrained translational and rotational motions and hydrogen bonding dynamics for all seven flavonoids.

The seven flavonoids share identical skeleton structures while varying in the saturation of ring C and the patterns of substituents. Among them, chrysin has the smallest molecular size and exhibits the lowest binding affinity toward TtgR. Taking chrysin as a reference, introducing alkyl substituents to rings A and C enhances van der Waals interactions with hydrophobic residues in the upper region of the binding pocket. However, the presence of a saturated ring C, as observed in naringenin, introduces steric effects that may interfere with its interaction with the hydrophilic residues. Simultaneously, the incorporation of hydroxyl groups onto ring B facilitates additional hydrogen bond formation with hydrophilic residues in the lower region of the active site. These structural modifications play crucial roles in modulating the specific interactions and binding affinity of the flavonoids with TtgR. For example, artocarpin contains two bulky alkyl groups on rings A and C and two hydroxyl groups at positions 2′ and 4′ of ring B. Accordingly, it exhibits a binding free energy that is 7.32 kcal/mol lower than chrysin, highlighting the impact of its larger size and specific substituent groups on enhancing favorable interactions with TtgR. Our computational predictions highlight the strong binding affinity of flavonoids to the TtgR transcriptional regular, providing valuable guidance for designing new biochemical and biophysical assays on this topic. These experimental investigations will explore the potential antimicrobial application of flavonoids against *P. putida* DOT-T1E and validate the accuracy of the computational results.

From our analyses, both aromaticity and the presence of hydroxyl substituent groups play important roles in facilitating the interactions between flavonoids and the TtgR transcriptional regulator. Interestingly, TtgR demonstrates a broad ligand specificity, exhibiting the capability to interact with compounds across diverse functional classes such as antibiotics, flavonoids, and organic solvents.[7,8,12] This broad specificity highlights the versatility of TtgR in recognizing and binding to a wide variety of small organic molecules, a characteristic integral to its role in regulating multidrug resistance in *P. putida* DOT-T1E. Despite variations in size and shape among its ligands, TtgR consistently demonstrates an affinity for molecules with aromatic components.[12] This feature allows the bacteria to respond and adapt to various toxic compounds present in their environment. Our findings thus offer valuable insight into potential molecular design strategies to address drug resistance in *P. putida* DOT-T1E, presenting new avenues for developing effective countermeasures against multidrug resistance in bacterial strains.

■ ASSOCIATED CONTENT

Ⓢ Supporting Information

The Supporting Information is available free of charge at https://pubs.acs.org/doi/10.1021/acs.jpcb.4c02303.

Additional computational methods, analysis of the AFE simulations, free energy surfaces for π stacking interactions, hydrogen bond analysis, and fitting parameters for the rotational and hydrogen bond time correlation functions (PDF)

■ AUTHOR INFORMATION

Corresponding Author

Lu Wang − *Department of Chemistry and Chemical Biology, Institute for Quantitative Biomedicine, Laboratory for Biomolecular Simulation Research, Rutgers University, Piscataway, New Jersey 08854, United States;* ⓞ orcid.org/0000-0001-6230-1835; Email: lwang@chem.rutgers.edu

Authors

Yuxuan Wu − *Department of Chemistry and Chemical Biology, Institute for Quantitative Biomedicine, Laboratory for Biomolecular Simulation Research, Rutgers University, Piscataway, New Jersey 08854, United States*

Shi Zhang − *Department of Chemistry and Chemical Biology, Institute for Quantitative Biomedicine, Laboratory for Biomolecular Simulation Research, Rutgers University, Piscataway, New Jersey 08854, United States*

Darrin M. York − *Department of Chemistry and Chemical Biology, Institute for Quantitative Biomedicine, Laboratory for Biomolecular Simulation Research, Rutgers University, Piscataway, New Jersey 08854, United States;* ⓞ orcid.org/0000-0002-9193-7055

Complete contact information is available at:
https://pubs.acs.org/10.1021/acs.jpcb.4c02303

Notes

The authors declare no competing financial interest.

■ REFERENCES

(1) Zgurskaya, H. I.; Nikaido, H. Multidrug resistance mechanisms: drug efflux across two membranes. *Mol. Microbiol.* **2000**, *37*, 219−225.

(2) Khameneh, B.; Diab, R.; Ghazvini, K.; Fazly Bazzaz, B. S. Breakthroughs in bacterial resistance mechanisms and the potential ways to combat them. *Microb. Pathog.* **2016**, *95*, 32−42.

(3) Du, D.; Wang-Kan, X.; Neuberger, A.; van Veen, H. W.; Pos, K. M.; Piddock, L. J. V.; Luisi, B. F. Multidrug efflux pumps: structure, function and regulation. *Nat. Rev. Microbiol.* **2018**, *16*, 523−539.

(4) Huang, L.; Wu, C.; Gao, H.; Xu, C.; Dai, M.; Huang, L.; Hao, H.; Wang, X.; Cheng, G. Bacterial Multidrug Efflux Pumps at the Frontline of Antimicrobial Resistance: An Overview. *Antibiotics* **2022**, *11*, 520.

(5) Ramos, J. L.; Duque, E.; Huertas, M.-J.; Haïdour, A. Isolation and expansion of the catabolic potential of a Pseudomonas putida strain able to grow in the presence of high concentrations of aromatic hydrocarbons. *J. Bacteriol.* **1995**, *177*, 3911−3916.

(6) Rojas, A.; Duque, E.; Mosqueda, G.; Golden, G.; Hurtado, A.; Ramos, J. L.; Segura, A. Three Efflux Pumps Are Required To Provide Efficient Tolerance to Toluene in *Pseudomonas putida* DOT-T1E. *J. Bacteriol.* **2001**, *183*, 3967−3973.

(7) Terán, W.; Krell, T.; Ramos, J. L.; Gallegos, M.-T. Effector-Repressor Interactions, Binding of a Single Effector Molecule to the Operator-bound TtgR Homodimer Mediates Derepression. *J. Biol. Chem.* 2006, 281, 7102−7109.

(8) Fernandez-Escamilla, A. M.; Fernandez-Ballester, G.; Morel, B.; Casares-Atienza, S.; Ramos, J. L. Molecular Binding Mechanism of TtgR Repressor to Antibiotics and Antimicrobials. *PLoS One* 2015, 10, No. e0138469.

(9) Vasylkivska, M.; Patakova, P. Role of efflux in enhancing butanol tolerance of bacteria. *J. Biotechnol.* 2020, 320, 17−27.

(10) Terán, W.; Felipe, A.; Segura, A.; Rojas, A.; Ramos, J.-L.; Gallegos, M.-T. Antibiotic-Dependent Induction of Pseudomonas putida DOT-T1E TtgABC Efflux Pump Is Mediated by the Drug Binding Repressor TtgR. *Antimicrob. Agents Chemother.* 2003, 47, 3067−3072.

(11) Yu, Z.; Reichheld, S. E.; Savchenko, A.; Parkinson, J.; Davidson, A. R. A Comprehensive Analysis of Structural and Sequence Conservation in the TetR Family Transcriptional Regulators. *J. Mol. Biol.* 2010, 400, 847−864.

(12) Alguel, Y.; Meng, C.; Terán, W.; Krell, T.; Ramos, J. L.; Gallegos, M.-T.; Zhang, X. Crystal Structures of Multidrug Binding Protein TtgR in Complex with Antibiotics and Plant Antimicrobials. *J. Mol. Biol.* 2007, 369, 829−840.

(13) Schrödinger. *Maestro*; LLC: New York, NY, 2023.

(14) Cushnie, T. T.; Lamb, A. J. Antimicrobial activity of flavonoids. *Int. J. Antimicrob. Agents* 2005, 26, 343−356.

(15) Panche, A. N.; Diwan, A. D.; Chandra, S. R. Flavonoids: an Overview. *J. Nutr. Sci.* 2016, 5, No. e47.

(16) Farhadi, F.; Khameneh, B.; Iranshahi, M.; Iranshahy, M. Antibacterial activity of flavonoids and their structure-activity relationship: An update review. *Phytother. Res.* 2019, 33, 13−40.

(17) Nguyen, T. L.; Bhattacharya, D. Antimicrobial Activity of Quercetin: An Approach to Its Mechanistic Principle. *Molecules* 2022, 27, 2494.

(18) Aleksandrov, A.; Simonson, T. Molecular mechanics models for tetracycline analogs. *J. Comput. Chem.* 2009, 30, 243−255.

(19) Sun, Z.; Wang, X.; Zhang, J. Z. H. Theoretical understanding of the thermodynamics and interactions in transcriptional regulator TtgR−ligand binding. *Phys. Chem. Chem. Phys.* 2020, 22, 1511−1524.

(20) Duarte, V. S.; Paula, R. L. G.; Custodio, J. M. F.; D'Oliveira, G. D. C.; Borges, L. L.; Pérez, C. N.; Perjesi, P.; Oliver, A. G.; Napolitano, H. B. A new quinolinone-chalcone hybrid with potential antibacterial and herbicidal properties using in silico approaches. *J. Mol. Model.* 2022, 28, 176.

(21) Leander, M.; Liu, Z.; Cui, Q.; Raman, S. Deep mutational scanning and machine learning reveal structural and molecular rules governing allosteric hotspots in homologous proteins. *eLife* 2022, 11, No. e79932.

(22) de Carvalho Matias, E. G.; Bezerra, K. S.; Costa, A. H. L.; Clemente Junior, W. S.; Oliveira, J. I. N.; Ribeiro Junior, L. A.; Galvão, D. S.; Fulco, U. L. Quantum biochemical analysis of the TtgR regulator and effectors. *Sci. Rep.* 2024, 14, 8519.

(23) Lucarini, R.; Tozatti, M.; Silva, M.; Gimenez, V.; Pauletti, P.; Groppo, M.; Turatti, I. C. C.; Cunha, W.; Martins, C. Antibacterial and anti-inflammatory activities of an extract, fractions, and compounds isolated from Gochnatia pulchra aerial parts. *Braz. J. Med. Biol. Res.* 2015, 48, 822−830.

(24) Lee, C.; Yang, W.; Parr, R. G. Development of the Colle-Salvetti correlation-energy formula into a functional of the electron density. *Phys. Rev. B: Condens Matter Mater. Phys.* 1988, 37, 785−789.

(25) Becke, A. D. Density-functional thermochemistry. III. The role of exact exchange. *J. Chem. Phys.* 1993, 98, 5648−5652.

(26) Frisch, M. J.; Trucks, G. W.; Schlegel, H. B.; Scuseria, G. E.; Robb, M. A.; Cheeseman, J. R.; Scalmani, G.; Barone, V.; Petersson, G. A.; Nakatsuji, H.; et al. *Gaussian 16, Revision A.03*; Gaussian Inc.: Wallingford CT, 2016.

(27) Eberhardt, J.; Santos-Martins, D.; Tillack, A. F.; Forli, S. AutoDock Vina 1.2.0: New Docking Methods, Expanded Force Field, and Python Bindings. *J. Chem. Inf. Model.* 2021, 61, 3891−3898.

(28) Case, D. A.; Cheatham, T. E.; Darden, T.; Gohlke, H.; Luo, R.; Merz, K. M.; Onufriev, A.; Simmerling, C.; Wang, B.; Woods, R. J. The Amber biomolecular simulation programs. *J. Comput. Chem.* 2005, 26, 1668−1688.

(29) Case, D.; Betz, R.; Cerutti, D.; Cheatham, T.; Darden, T.; Duke, R.; Giese, T.; Gohlke, H.; Goetz, A.; Homeyer, N.; et al. *Amber 2016*; University of California: San Francisco, 2016.

(30) Maier, J. A.; Martinez, C.; Kasavajhala, K.; Wickstrom, L.; Hauser, K. E.; Simmerling, C. ff14SB: Improving the Accuracy of Protein Side Chain and Backbone Parameters from ff99SB. *J. Chem. Theory Comput.* 2015, 11, 3696−3713.

(31) Wang, J.; Wolf, R. M.; Caldwell, J. W.; Kollman, P. A.; Case, D. A. Development and testing of a general amber force field. *J. Comput. Chem.* 2004, 25, 1157−1174.

(32) Jorgensen, W. L.; Chandrasekhar, J.; Madura, J. D.; Impey, R. W.; Klein, M. L. Comparison of simple potential functions for simulating liquid water. *J. Chem. Phys.* 1983, 79, 926−935.

(33) Loncharich, R. J.; Brooks, B. R.; Pastor, R. W. Langevin dynamics of peptides: The frictional dependence of isomerization rates of N-acetylalanyl-N'-methylamide. *Biopolymers* 1992, 32, 523−535.

(34) Berendsen, H. J. C.; Postma, J. P. M.; Van Gunsteren, W. F.; DiNola, A.; Haak, J. R. Molecular dynamics with coupling to an external bath. *J. Chem. Phys.* 1984, 81, 3684−3690.

(35) Darden, T.; York, D.; Pedersen, L. Particle mesh Ewald: An Nlog (N) method for Ewald sums in large systems. *J. Chem. Phys.* 1993, 98, 10089−10092.

(36) Hess, B.; Bekker, H.; Berendsen, H. J. C.; Fraaije, J. G. E. M. LINCS: A linear constraint solver for molecular simulations. *J. Comput. Chem.* 1997, 18, 1463−1472.

(37) Jorgensen, W. L. Efficient Drug Lead Discovery and Optimization. *Acc. Chem. Res.* 2009, 42, 724−733.

(38) Chodera, J. D.; Mobley, D. L.; Shirts, M. R.; Dixon, R. W.; Branson, K.; Pande, V. S. Alchemical free energy methods for drug discovery: progress and challenges. *Curr. Opin. Struct. Biol.* 2011, 21, 150−160.

(39) Mobley, D. L.; Klimovich, P. V. Perspective: Alchemical free energy calculations for drug discovery. *J. Chem. Phys.* 2012, 137, 230901.

(40) Abel, R.; Wang, L.; Harder, E. D.; Berne, B. J.; Friesner, R. A. Advancing Drug Discovery through Enhanced Free Energy Calculations. *Acc. Chem. Res.* 2017, 50, 1625−1632.

(41) Cournia, Z.; Allen, B.; Sherman, W. Relative Binding Free Energy Calculations in Drug Discovery: Recent Advances and Practical Considerations. *J. Chem. Inf. Model.* 2017, 57, 2911−2937.

(42) Wan, S.; Bhati, A. P.; Zasada, S. J.; Coveney, P. V. Rapid, accurate, precise and reproducible ligand−protein binding free energy prediction. *Interface Focus* 2020, 10, 20200007.

(43) Lee, T.-S.; Allen, B. K.; Giese, T. J.; Guo, Z.; Li, P.; Lin, C.; McGee, T. D.; Pearlman, D. A.; Radak, B. K.; Tao, Y.; et al. Alchemical Binding Free Energy Calculations in AMBER20: Advances and Best Practices for Drug Discovery. *J. Chem. Inf. Model.* 2020, 60, 5595−5623.

(44) Jia, X.; Ge, H.; Mei, Y. Free energy change estimation: The Divide and Conquer MBAR method. *J. Comput. Chem.* 2021, 42, 1204−1211.

(45) York, D. M. Modern Alchemical Free Energy Methods for Drug Discovery Explained. *ACS Phys. Chem. Au* 2023, 3, 478−491.

(46) Papadourakis, M.; Sinenka, H.; Matricon, P.; Hénin, J.; Brannigan, G.; Pérez-Benito, L.; Pande, V.; van Vlijmen, H.; de Graaf, C.; Deflorian, F.; et al. Alchemical Free Energy Calculations on Membrane-Associated Proteins. *J. Chem. Theory Comput.* 2023, 19, 7437−7458.

(47) Chen, L.; Wu, Y.; Wu, C.; Silveira, A.; Sherman, W.; Xu, H.; Gallicchio, E. Performance and Analysis of the Alchemical Transfer Method for Binding-Free-Energy Predictions of Diverse Ligands. *J. Chem. Inf. Model.* 2024, 64, 250−264.

(48) Khuttan, S.; Gallicchio, E. What to Make of Zero: Resolving the Statistical Noise from Conformational Reorganization in Alchemical

Binding Free Energy Estimates with Metadynamics Sampling. *J. Chem. Theory Comput.* **2024**, *20*, 1489−1501.

(49) Wang, S.; Liu, F.; Li, P.; Wang, J.-N.; Mo, Y.; Lin, B.; Mei, Y. Potent inhibitors targeting cyclin-dependent kinase 9 discovered via virtual high-throughput screening and absolute binding free energy calculations. *Phys. Chem. Chem. Phys.* **2024**, *26*, 5377−5386.

(50) Case, D. A.; Aktulga, H. M.; Belfon, K.; Ben-Shalom, I. Y.; Berryman, J. T.; Brozell, S. R.; Cerutti, D. S.; Cheatham III, T. E.; Cisneros, G. A.; Cruzeiro, V. W. D.; et al. *Amber 2022*; University of California: San Francisco, 2022.

(51) Lee, T.-S.; Tsai, H.-C.; Ganguly, A.; Giese, T. J.; York, D. M. *Free Energy Methods in Drug Discovery: Current State and Future Directions*; ACS Symposium Series; 2021; Vol *1397*, Chapter 7, pp 161−204.

(52) Lee, T.-S.; Cerutti, D. S.; Mermelstein, D.; Lin, C.; LeGrand, S.; Giese, T. J.; Roitberg, A.; Case, D. A.; Walker, R. C.; York, D. M. GPU-Accelerated Molecular Dynamics and Free Energy Methods in Amber18: Performance Enhancements and New Features. *J. Chem. Inf. Model.* **2018**, *58*, 2043−2050.

(53) Giese, T. J.; York, D. M. A GPU-Accelerated Parameter Interpolation Thermodynamic Integration Free Energy Method. *J. Chem. Theory Comput.* **2018**, *14*, 1564−1582.

(54) Kirkwood, J. G. Statistical Mechanics of Fluid Mixtures. *J. Chem. Phys.* **1935**, *3*, 300−313.

(55) Straatsma, T. P.; Berendsen, H. J. C. Free energy of ionic hydration: Analysis of a thermodynamic integration technique to evaluate free energy differences by molecular dynamics simulations. *J. Chem. Phys.* **1988**, *89*, 5876−5886.

(56) Lee, T.-S.; Lin, Z.; Allen, B. K.; Lin, C.; Radak, B. K.; Tao, Y.; Tsai, H.-C.; Sherman, W.; York, D. M. Improved Alchemical Free Energy Calculations with Optimized Smoothstep Softcore Potentials. *J. Chem. Theory Comput.* **2020**, *16*, 5512−5525.

(57) Tsai, H.-C.; Lee, T.-S.; Ganguly, A.; Giese, T. J.; Ebert, M. C. C. J. C.; Labute, P.; Merz Jr, K. M.; York, D. M. AMBER Free Energy Tools: A New Framework for the Design of Optimized Alchemical Transformation Pathways. *J. Chem. Theory Comput.* **2023**, *19*, 640−658.

(58) Ganguly, A.; Tsai, H.-C.; Fernández-Pendás, M.; Lee, T.-S.; Giese, T. J.; York, D. M. AMBER Drug Discovery Boost Tools: Automated Workflow for Production Free-Energy Simulation Setup and Analysis (ProFESSA). *J. Chem. Inf. Model.* **2022**, *62*, 6069−6083.

(59) Lee, T.-S.; Tsai, H.-C.; Ganguly, A.; York, D. M. ACES: Optimized Alchemically Enhanced Sampling. *J. Chem. Theory Comput.* **2023**, *19*, 472−487.

(60) He, X.; Man, V. H.; Yang, W.; Lee, T.-S.; Wang, J. A fast and high-quality charge model for the next generation general AMBER force field. *J. Chem. Phys.* **2020**, *153*, 114502.

(61) Horn, H. W.; Swope, W. C.; Pitera, J. W.; Madura, J. D.; Dick, T. J.; Hura, G. L.; Head-Gordon, T. Development of an improved four-site water model for biomolecular simulations: TIP4P-Ew. *J. Chem. Phys.* **2004**, *120*, 9665−9678.

(62) Åqvist, J.; Wennerström, P.; Nervall, M.; Bjelic, S.; Brandsdal, B. O. Molecular dynamics simulations of water and biomolecules with a Monte Carlo constant pressure algorithm. *Chem. Phys. Lett.* **2004**, *384*, 288−294.

(63) Case, D. A.; Aktulga, H. M.; Belfon, K.; Cerutti, D. S.; Cisneros, G. A.; Cruzeiro, V. W. D.; Forouzesh, N.; Giese, T. J.; Götz, A. W.; Gohlke, H.; et al. AmberTools. *J. Chem. Inf. Model.* **2023**, *63*, 6183−6191.

(64) Shirts, M. R.; Pande, V. S. Comparison of efficiency and bias of free energies computed by exponential averaging, the Bennett acceptance ratio, and thermodynamic integration. *J. Chem. Phys.* **2005**, *122*, 144107.

(65) Shirts, M. R.; Chodera, J. D. Statistically optimal analysis of samples from multiple equilibrium states. *J. Chem. Phys.* **2008**, *129*, 124105.

(66) Klimovich, P. V.; Shirts, M. R.; Mobley, D. L. Guidelines for the analysis of free energy calculations. *J. Comput. Aided Mol. Des.* **2015**, *29*, 397−411.

(67) Giese, T. J.; York, D. M. Variational Method for Networkwide Analysis of Relative Ligand Binding Free Energies with Loop Closure and Experimental Constraints. *J. Chem. Theory Comput.* **2021**, *17*, 1326−1336.

(68) Wang, J.; Yao, L. Dissecting C−H•••π and N−H•••π Interactions in Two Proteins Using a Combined Experimental and Computational Approach. *Sci. Rep.* **2019**, *9*, 20149.

(69) Nishio, M. CH/π hydrogen bonds in crystals. *CrystEngComm* **2004**, *6*, 130−158.